Journal of Materials Science & Technology 157 (2023) 30–41

Contents lists available at ScienceDirect

Journal of Materials Science & Technology

journal homepage: www.elsevier.com/locate/jmst

Research Article

Simultaneously improving mechanical properties and oxidation resistance of Ti-bearing high-entropy superalloys at intermediate temperature via silicon addition

Shaofei Liu[a,b], Weicheng Xiao[a,c], Bo Xiao[b,c], Jiang Ju[b,c], Yinghao Zhou[b,c], Yilu Zhao[d], Zengbao Jiao[e], Junhua Luan[c], Qian Li[c], Jinxiong Hou[c], Ji-jung Kai[a,b,f,*], Tao Yang[c,f,*]

[a] Department of Mechanical Engineering, City University of Hong Kong, Hong Kong 999077, China
[b] Center for Advanced Nuclear Safety and Sustainable Development, City University of Hong Kong, Hong Kong 999077, China
[c] Department of Materials Science and Engineering, City University of Hong Kong, Hong Kong 999077, China
[d] School of Materials Science and Engineering, Harbin Institute of Technology, Shenzhen 518055, China
[e] Department of Mechanical Engineering, The Hong Kong Polytechnic University, Hong Kong 999077, China
[f] Hong Kong Institute for Advanced Study, City University of Hong Kong, Hong Kong 999077, China

ARTICLE INFO

Article history:
Received 24 November 2022
Revised 28 December 2022
Accepted 4 January 2023
Available online 25 March 2023

Keywords:
High-entropy superalloy
Mechanical property
Oxidation behavior
Intermediate temperature
Silicon addition

ABSTRACT

Ti-bearing high-entropy superalloys (HESAs) often suffer from severe intergranular embrittlement and terrible oxidation degradation at intermediate temperatures. Here we showcase that minor Si addition can effectively mitigate the intergranular embrittlement and improve the oxidation resistance of the a $(Ni_2Co_2FeCr)_{92}Ti_4Al_4$ HESA at 700 °C simultaneously. Experimental analysis revealed that the intergranular G phase induced by 2 at% Si addition can effectively suppress the inward diffusion of oxygen along grain boundaries at 700 °C, thus enhancing the tensile ductility of the alloy from ~8.3% to ~13.4%. Besides, the 2 at% Si addition facilitated the formation of a continuous Al_2O_3 layer during oxidation, contributing to a remarkable reduction in the growth rate of the oxide scale to a quarter of the Si-free HESA. Our results demonstrate that Si can be a favorable alloying element to design advanced HESAs with synergistically improved thermal-mechanical performance.

1. Introduction

As a promising material design concept, high-entropy alloys (HEAs) provide a near-infinite multicomponent phase space that can bring about various attractive properties, rendering them promising candidates as high-performance structural components [1–5]. Of particular interest, $L1_2$-strengthened HEAs, also known as high-entropy superalloys (HESAs), are regarded as potential alternatives for heat-resistant materials owing to their similar microstructure to that of Ni-based superalloys, that is, the ductile face-centered-cubic (FCC) matrix together with the coherently embedded $L1_2$ nanoparticles [6–10]. Among the HESAs, Ti-bearing systems have attracted substantial interest due to their excellent mechanical performances in a wide temperature window and remarkable thermal stability [11–16]. During deformation, the high lattice distortion of the FCC matrix and the high lattice mismatch between the FCC matrix and $L1_2$ nanoparticles in the Ti-bearing HESAs endow them with high strength [17,18]. At elevated temperatures, Ti-bearing HESAs manifest superior strength even surpassing that of conventional Ni-based superalloys [6,13,19]. For instance, Yang et al. [13] reported that superb tensile strengths of above 800 MPa can be achieved at 700 °C in a Ni-30Co-13Fe-15Cr-6Al-6Ti-0.1B (at%) HESA, which is higher than that of commercial Ni-based Inconel 617 and Alloy 800H. Meanwhile, the extremely small interfacial energies render the Ti-bearing HESAs extraordinarily sluggish coarsening behavior of the coherent $L1_2$ nanoprecipitates. For example, the coarsening rate of $L1_2$ nanoprecipitates in the $(NiCoFeCr)_{94}Ti_2Al_4$ HESA is only a quarter of that of commercial Nimonic PE16 at 800 °C [15]. Combining the above two merits, Ti-bearing HESAs exhibit enormous potential for engineering applications at intermediate temperatures.

However, the Ti-bearing HESAs still suffer from two severe problems at intermediate-temperature regions, i.e., intergranular embrittlement and oxidation degradation. On the one hand, the grain boundaries (GBs) of most existing polycrystalline HESAs are generally susceptible to oxygen penetration when tension at 600–

* Corresponding authors.
E-mail addresses: jijkai@cityu.edu.hk (J.-j. Kai), taoyang6-c@my.cityu.edu.hk (T. Yang).

https://doi.org/10.1016/j.jmst.2023.01.044
1005-0302/

800 °C [9,13,20]. The resultant premature failure upon tensile deformation due to GB decohesion seriously limits the elevated-temperature engineering applications. On the other hand, during long-term exposure at elevated temperatures, the diffusion of Ti ions through corundum scales brings about excessive vacancies, thus enhancing the overall oxidation rates by promoting the outward diffusion of cations [21,22]. The dealloying corrosion and surface strength loss accompanying the severe oxidation may facilitate the crack initiation upon stress, thus posing a serious threat to the service life of structural components [23–25].

Previous studies have demonstrated that enhanced mechanical properties and oxidation resistance can be simultaneously achieved at intermediate temperatures by tailoring the chemical compositions of Ti-bearing HESAs [20,21]. For example, increasing the Cr concentration in $Ni_{39.9}Co_{20}Fe_{30-x}Cr_xAl_6Ti_4B_{0.1}$ HESAs can effectively promote the formation of a compact Cr_2O_3 layer at 600 °C, significantly hindering the oxygen penetration along GBs and thus substantially improving the tensile ductility [20]. Meanwhile, the substitution of Ti by Nb in a $(Ni_2Co_2FeCr)_{92}Ti_4Al_4$ HESA brings about a significantly improved oxidation resistance by five times and a slightly increased tensile ductility at 700 °C [21]. Nevertheless, the HESAs optimized by the above strategies are still faced with several challenges. First, without other types of antioxidant elements, the oxidation resistance of Ti-bearing HESAs with high Cr concentrations is still insufficient upon prolonged exposure at elevated temperatures, resulting from the high diffusivity of Ti ions in the Cr_2O_3 oxide [21,26]. Second, Nb-containing $L1_2$-precipitates tend to transform into an ε phase above 800 °C, inhibiting the practical application of Nb-bearing HESAs at higher temperatures [27]. Third, these HESAs still suffer from low tensile ductility, typically < 10% elongation, at temperatures of higher than 600 °C [9,13,21]. Therefore, further compositional optimization is necessary to realize superior mechanical properties and oxidation resistance in Ti-bearing HESAs.

Among the various compositional tailoring schemes, Si was well demonstrated to be an effective alloying element to improve the mechanical properties and oxidation resistance of HEAs [28–32]. It has been reported that Si additions can optimize the mechanical performances of FCC HEAs by solid solution strengthening and reducing stacking fault energies (SFEs) [28,29]. Besides, several studies have been conducted to investigate the effect of Si on the oxidation behavior of HEAs with different microstructures, including FCC [30], body-cubic-centered (BCC) [31], and eutectic systems [32]. The results revealed that during long-term exposure, proper addition of Si promotes the formation of a protective SiO_2 or Si-containing amorphous oxide layer, thus preventing the inward diffusion of oxygen. However, the influence of Si on the tensile ductility and oxidation resistance of Ti-bearing HESAs at intermediate temperatures has rarely been systematically investigated so far, even though it is important for properly designing HESAs with enhanced high-temperature performance.

In the present work, we selected a $(Ni_2Co_2FeCr)_{92}Ti_4Al_4$ HESA to be a model alloy. Si was introduced and a series of $(Ni_2Co_2FeCr)_{92-x}Ti_4Al_4Si_x$ (x = 0, 1, and 2 at%) alloys were fabricated. All the alloy microstructures (e.g., phase constitutions and distribution) were carefully characterized. Specifically, the tensile response and oxidation behavior of the alloys at 700 °C were evaluated in great detail to gain insights into the feasibility of improving the strength-ductility combination and oxidation resistance at intermediate temperatures by Si addition.

2. Experimental

The $(Ni_2Co_2FeCr)_{92-x}Ti_4Al_4Si_x$ (x = 0, 1, and 2 at%) HESAs ingots were fabricated in an arc-melting furnace filled with high-purity argon. The three studied HESAs are hereafter termed 0Si-HESA, 1Si-HESA, and 2Si-HESA for simplicity's sake. During arc-melting, the mixture of raw metals with purities of higher than 99.9 wt% was flipped and re-melted six times to reduce compositional inhomogeneity. The obtained ingots were then drop-cast into slabs with a dimension of 100 mm × 12 mm × 5 mm in a water-cooled copper mold. After that, the slabs were homogenized at 1200 °C for 2 h, followed by cold rolling of ~65% thickness reduction and then a recrystallization treatment at 1160 °C for 2 min. Subsequently, $L1_2$-nanoprecipitates were introduced in the alloys by isothermal aging at 800 °C for 24 h.

Tensile tests were implemented employing a Material Testing System (MTS) tension machine with a strain rate of 10^{-3} s^{-1} at 700 °C. Dog-bone-shaped specimens with a gauge size of 12.5 mm length, 3.2 mm width, and 1.5 mm thickness were taken along the rolling direction from the aged sheets by electro-discharging machining. Each side of the specimens was carefully mechanically grounded down to 2000-grit finish with SiC paper. To eliminate temperature fluctuation during the elevated temperature tensile tests, tensile specimens were placed in an electric furnace for an additional 10 min at the testing temperature before tests.

Prior to the oxidation test, square coupons with a dimension of 10 mm × 10 mm × 1.7 mm were sectioned from the aged samples by electro-discharge machining. Then all surfaces of the samples were mechanically grounded to 4500-grit with SiC papers, followed by ultrasonic cleaning with absolute ethanol. Isothermal cyclic oxidation tests were conducted in a conventional resistance muffle furnace at 700 °C up to 480 h. The specimens were got out from the furnace to record the weights after a specific oxidation period and then calculate their weight changes before and after the oxidation test.

Phase structures of the alloys before and after oxidation were identified by X-ray diffraction (XRD, Rigaku) equipped with a monochromator. Scanning electron microscope (SEM, Quanta FEG450) and transmission electron microscopy (TEM, JEM-2100F) were used to characterize the microstructures. Composition analyses were performed with TEM and atom probe tomography (APT, CAMECA LEAP 5000XR) equipped with an energy dispersive spectrometer (EDS). TEM and APT samples were fabricated using the ion milling and lift-out technique in a focused ion beam/scanning electron microscope (FIB/SEM, FEI Scios) system.

3. Results

3.1. Initial microstructure

The initial structures of the studied HESAs were identified by XRD and SEM, as shown in Fig. 1. The XRD results in Fig. 1(a_1–a_3) reveal that only FCC and $L1_2$ peaks can be observed for all the HESAs. The representative SEM images in Fig. 2(a_1–a_3) show that the addition of Si has no significant influence on the grain size of the HESAs, evidenced by the similar grain sizes of about 60 μm determined by the linear intercept method for all the studied alloys. After being aged for 24 h at 800 °C, a typical dual-phase "$L1_2$ + FCC" microstructure, i.e., high-density spheroidal continuous $L1_2$-precipitates embedded in the FCC matrix, was formed in the grain interiors of all HESAs (Fig. 3(a_1–a_3)). The volume fractions of the $L1_2$-precipitates were estimated to be 23.6%, 23.8%, and 19.6% by CALculation of PHAse Diagrams (CALPHAD) method (see Supplementary Materials) for the 0Si-HESA, 1Si-HESA, and 2Si-HESA, respectively. Notably, remarkable differences in the GB morphologies are found in the HESAs with different Si contents. For the 0Si-HESA and 1Si-HESA, abundant $L1_2$-type discontinuous precipitates (DPs) with lamellar-like or short-rods shapes can be observed in the vicinity of GBs (Fig. 1(c_1, c_2)). These DPs grow by consuming the matrix near the initial GBs to form a classical double-seam morphology, similar to several existing Ti-bearing

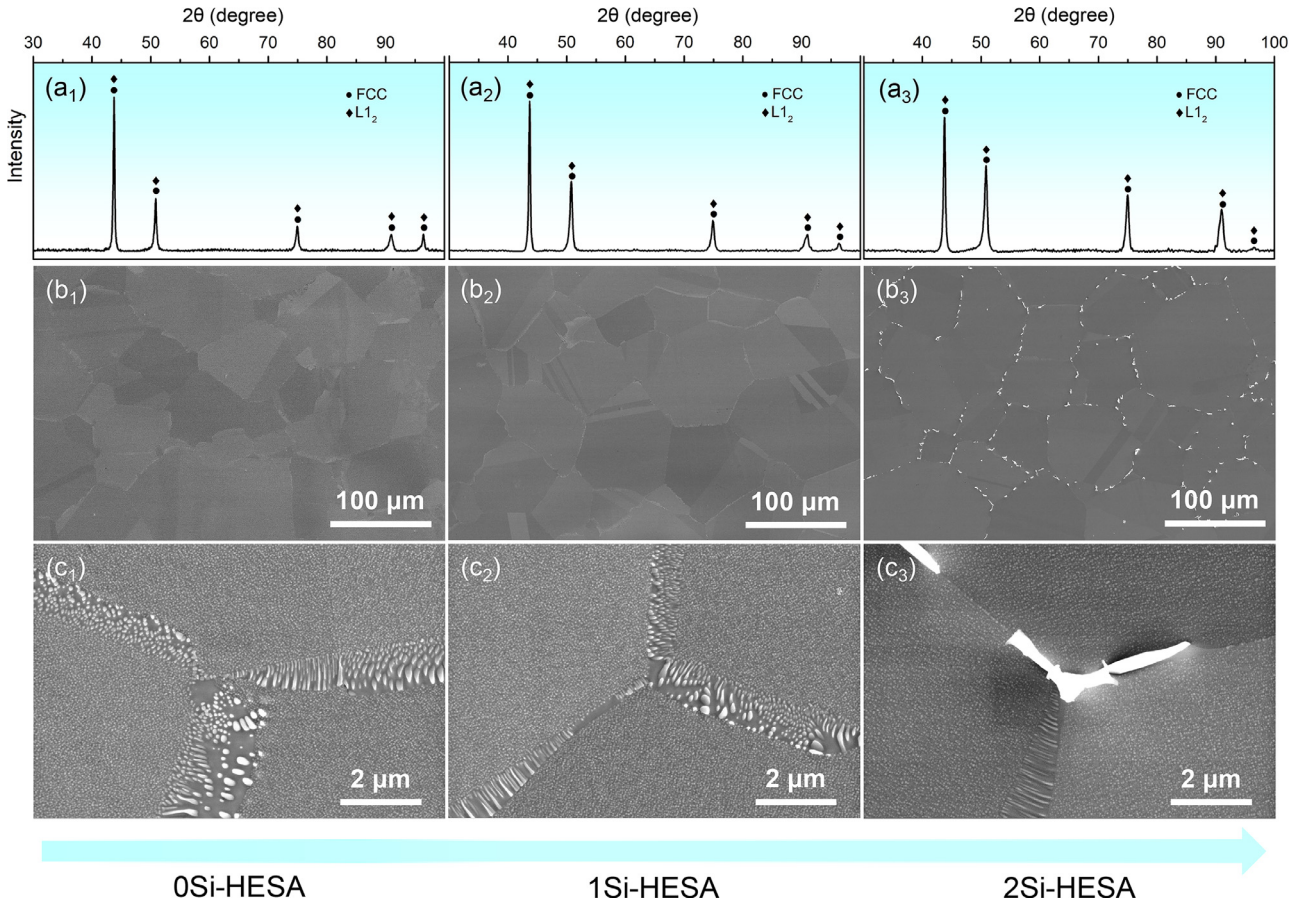

Fig. 1. (a_1–a_3) XRD patterns, (b_1–b_3) low-magnification SEM images, and (c_1–c_3) high-magnification SEM images of the as-fabricated HESAs with different Si contents.

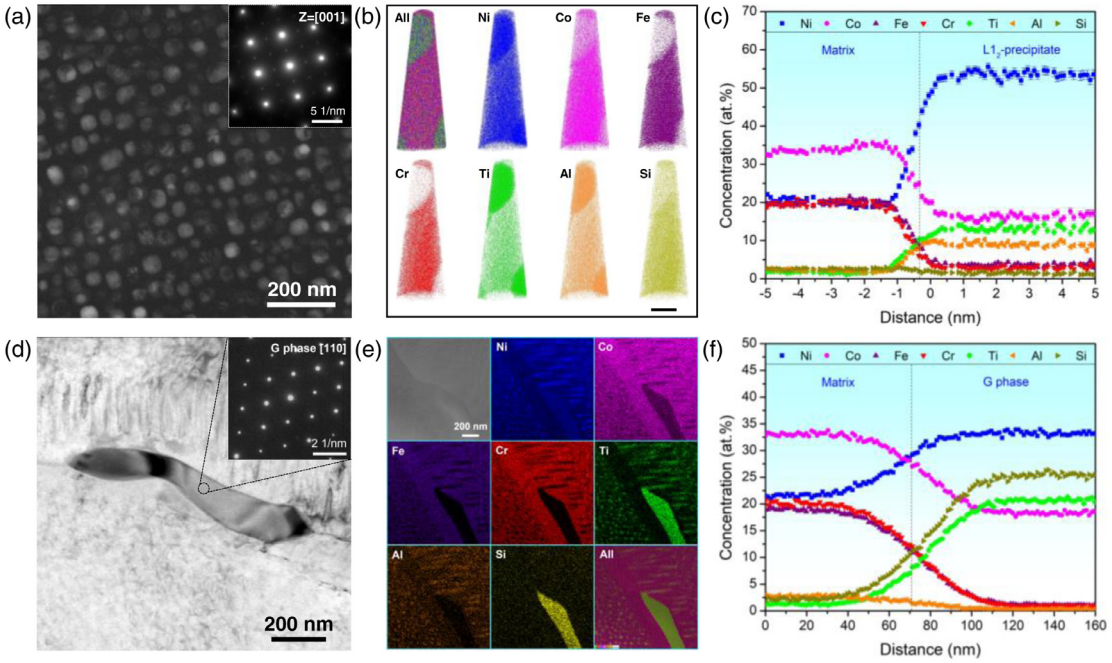

Fig. 2. Microstructures of the GB and grain interior of the 2Si-HESA: (a) DF-TEM image showing the $L1_2$-precipitates distribution. (b) APT maps showing the elemental partitioning between the matrix and $L1_2$-precipitates. Scale bar, 20 nm. (c) Proximity histogram across the interfaces between the matrix and $L1_2$-nanoparticles. (d) BF-TEM image showing the intergranular precipitate and the corresponding SADP. (e) STEM-EDS mapping displaying the elemental distribution of the intergranular precipitate. (f) STEM-EDS line-scanning profiles across the matrix and the intergranular precipitate.

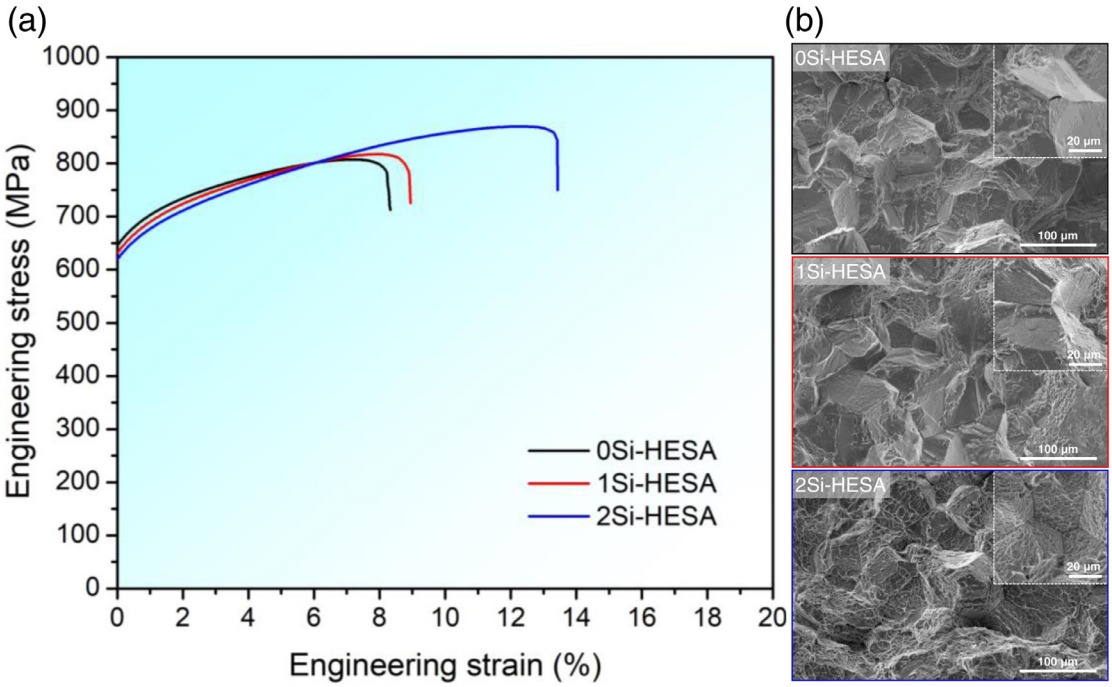

Fig. 3. (a) Uniaxial tensile curves and (b) the corresponding SEM fractographic images of the studied HESAs tested at 700 °C in air.

Table 1
Chemical compositions of different phases in the 2Si-HESA.

Phases	Concentration (at.%)						
	Ni	Co	Fe	Cr	Ti	Al	Si
Matrix	20.16 ± 0.93	33.84 ± 0.85	20.07 ± 0.55	19.68 ± 0.52	1.63 ± 0.22	2.12 ± 0.28	2.49 ± 0.20
$L1_2$-precipitate	53.62 ± 0.90	16.26 ± 0.72	3.66 ± 0.37	2.91 ± 0.40	13.12 ± 0.68	9.01 ± 0.58	1.42 ± 0.26
G phase	33.26 ± 0.33	18.28 ± 0.26	1.13 ± 0.08	0.89 ± 0.07	20.63 ± 0.28	0.31 ± 0.11	25.50 ± 0.37

HESAs [16,33,34]. With the Si concentration increasing to 2 at%, additional blocky precipitates with micron sizes are found to be irregularly dispersed along GBs (Fig. 1(b_3, c_3)). These intergranular-type precipitates are predicted to be G phase by CALPHAD (see Supplementary Materials).

The initial microstructure of the 2Si-HESA was further characterized by TEM and APT, as shown in Fig. 2. Representative dark-field (DF) TEM images in Fig. 2(a) reveal the distribution of the spherical $L1_2$-precipitates in the grain interior of the 2Si-HESA. The inserted superlattice spots in the selected area diffraction pattern (SADP) recorded at the [001] zone axis manifest the $L1_2$-ordered structure of the nanoprecipitates. Atom maps of all elements analyzed by APT, and corresponding quantitative proximity histograms across the interface between the FCC matrix and $L1_2$-precipitates are presented in Fig. 2(b, c), respectively. Obviously, Ni, Ti, and Al are partitioned to the $L1_2$-precipitates significantly, whereas Co and Si are marginally depleted and Fe and Cr are strongly depleted. The detailed elemental composition of each phase is summarized in Table 1. Meanwhile, the TEM-EDS results in Fig. 2(d, e) further reveal the morphology and chemical composition of the intergranular particles in 2Si-HESA. In the bright-field (BF) TEM image, an irregular-shaped intergranular precipitate can be clearly observed (Fig. 2(d)). The inserted SADP further identifies the nature of the FCC-type G phase of the intergranular precipitate. Based on the STEM-EDS mapping analysis (Fig. 2(e)), the intergranular precipitate is enriched with Ni, Ti, and Si, which is further determined to be $(NiCo)_{16}Si_7Ti_6$-type G phase by EDS line-scanning analysis (Fig. 2(f)). The detailed composition of the G phase is also listed in Table 1.

3.2. Mechanical properties and deformation microstructures

Representative engineering stress–strain curves for the three HESAs tested at 700 °C are displayed in Fig. 3(a). With the 2 at% Si addition, the yield strengths of the HESAs decrease slightly from 645 to 619 MPa, resulting from the reduced volume fraction of $L1_2$ precipitates. However, simultaneously enhanced ultimate tensile strength and ductility are revealed in the Si-doped HESAs. Compared with the 0Si-HESA, the ultimate tensile strength of the 2Si-HESA increased from 808 to 870 MPa, while the ductility improved from ~8.2% to ~13.4%. The SEM fractography of the 0Si-HESA and 1Si-HESA in Fig. 3(b) presents a fully intergranular fracture mode, as evidenced by the massive smooth cleavage facets on the fracture surfaces. Although also dominated by the intergranular fracture mode, the decoration of abundant fine dimples on the cleavage facets of the 2Si-HESA indicates the stronger GB cohesion at 700 °C.

Representative TEM images of the deformed 0Si-HESA and 2Si-HESA are shown in Fig. 4. Clearly, parallel sets of stacking faults (SFs) along the (111) slip planes can be observed in both alloys (Fig. 4(a, b)). The SFs reveal intermittent configurations, and their extension is thought to be blocked at the matrix/$L1_2$-precipitates interfaces. This indicates that the $L1_2$ nanoprecipitates serve as strong barriers toward dislocation movement, which is the dom-

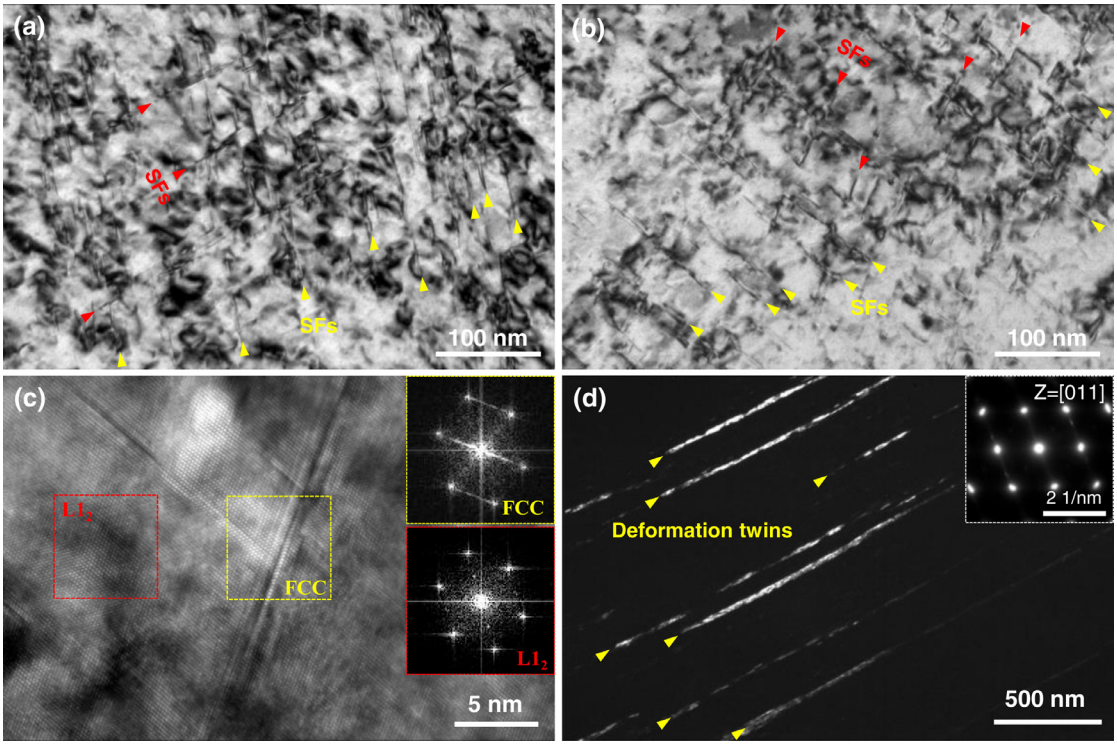

Fig. 4. Bright-field TEM micrographs displaying the deformation microstructures of the fractured (a) 0Si-HESA and (b) 2Si-HESA. (c) Representative HR-TEM image of SFs in (b). (d) Dark-field TEM image and corresponding SADP indicating the occurrence of deformation twinning in the 2Si-HESA.

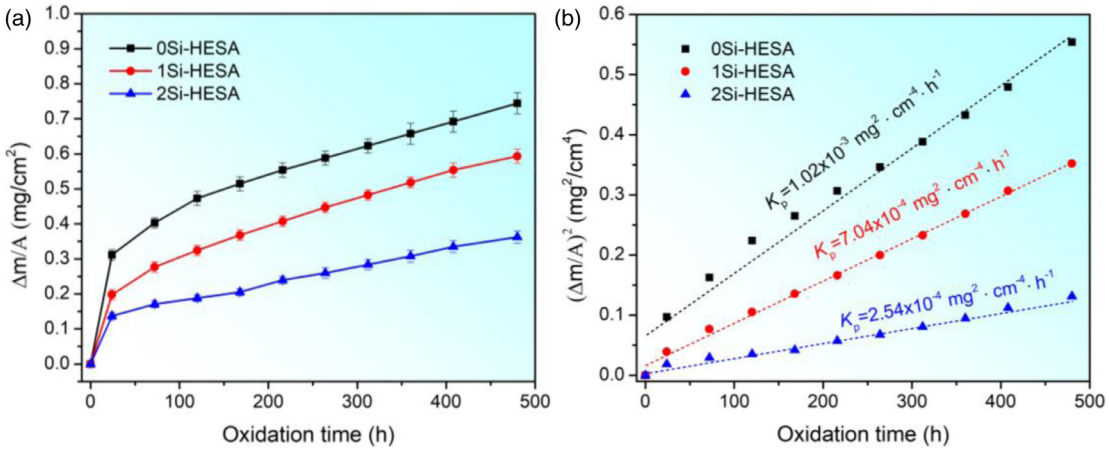

Fig. 5. Oxidation kinetics curves of the three studied HESAs after the exposure at 700 °C up to 480 h: (a) mass gains plots and (b) fitted lines of squared mass gain.

inant strengthening mechanism at the current deformation temperature. The high-resolution (HR) TEM image in Fig. 4(c) further gives a close-up view of the SFs of the 2Si-HESA. The inserted fast Fourier transform (FFT) patterns also indicate that the FCC matrix is sheared by SFs. Notably, in addition to SFs, a few grains of the 2Si-HESA underwent twinning as part of the deformation process. The TEM images in Fig. 4(d) and the corresponding SADP clearly capture deformation twins with an average thickness of ~25 nm. Micro-twins are normally found in superalloys with low SFEs during deformation at elevated temperatures [35]. In previous studies, Si additions have been widely demonstrated to reduce the SFEs of FCC-type HEAs, especially at elevated temperatures due to the potential Suzuki segregation of Si atoms to stacking faults [36]. Meanwhile, the intergranular precipitation of the G phase in the current study depletes Ni in the FCC matrix (Fig. 2), therefore further decreasing the SFE. Hence, it is reasonable to deduce that the occurrence of deformation twinning in the 2Si-HESA can be attributed to the reduced SFE via Si addition.

3.3. Oxidation kinetics

The mass-change curves of the studied HESAs after exposure at 700 °C for 480 h are displayed in Fig. 5(a). The mass gain per area increased with the exposure time and no spallation was found for all the HESAs. Apparently, the mass gain value decreases with the increased Si content in the HESAs. After the 480-h oxidation at 700 °C, the total mass gains per area are measured to be 0.74, 0.59, and 0.36 mg cm^{-2} for the 0Si-HESA, 1Si-HESA, and 2Si-HESA, respectively. This indicates a significantly improved oxidation resistance by increasing the Si concentration of the Ti-bearing HESAs. Fig. 5(b) displays the relationship between the square of mass gain and oxidation time of the three HESAs. The oxidation kinetics of the three HESAs follow a parabolic-rate law, as expressed by the

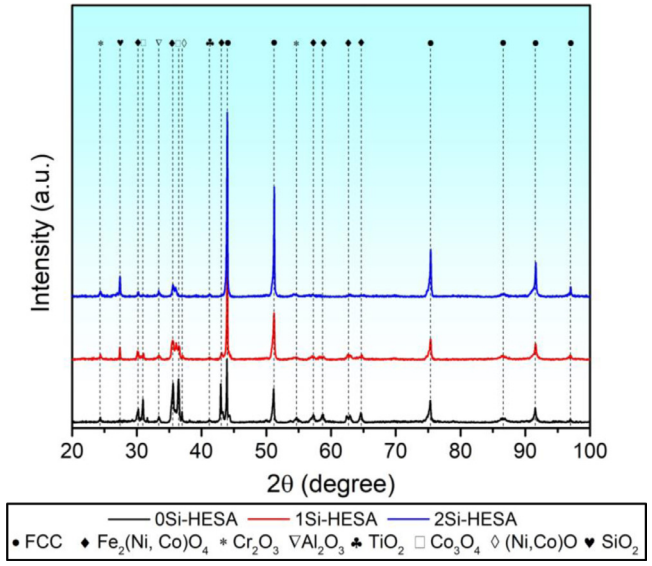

Fig. 6. XRD patterns of the three studied HESAs after oxidation at 700 °C for 480 h.

following equation [37]:

$$(\Delta m/A)^2 = k_p t + C \quad (1)$$

where $\Delta m/A$ is the mass gain per unit area of the oxidized samples, k_p represents the parabolic rate constant, t is the corresponding exposure time, and C is a constant. The linear fit to the square of mass gain vs oxidation time for the three HESAs is also exhibited in Fig. 5(b). After adding 1 at% Si to the initial alloy, the k_p value decreases from 1.02×10^{-3} mg^2 cm^{-4} h^{-1} for the 0Si-HESA to 7.04×10^{-4} mg^2 cm^{-4} h^{-1} for the 1Si-HESA. Among the three HESAs, the 2Si-HESA displays the lowest k_p value, which is only a quarter of the 0Si-HESA, i.e., 2.54×10^{-4} mg^2 cm^{-4} h^{-1}. The oxidation resistance of the 2Si-HESA is comparable to the commercial Inconel 617 and Inconel 738 superalloys, indicating its potential application as practical structural materials [38].

3.4. Microstructure of the HESAs after long-term oxidation

3.4.1. Phase identification

Fig. 6 comparatively exhibits the XRD profiles conducted on the surface of the three oxidized HESAs. The recognition of FCC peaks derived from the matrix indicates that the oxide layers from outside to the inside of all three HESAs can be well identified by XRD. With the Si additions, the intensity of FCC peaks increases, implying the decreased thickness of the oxide scale. After the oxidation at 700 °C for 480 h, diffraction peaks corresponding to $Fe_2(Ni,Co)O_4$, Cr_2O_3, Al_2O_3, and TiO_2 can be observed in all three HESAs. In addition, NiO and Co_3O_4 can be identified in the 0Si-HESA and 1Si-HESA, and the corresponding diffraction intensity decreases with the addition of Si. Notably, diffraction peaks of NiO and Co_3O_4 are missing in the 2Si-HESA. Meanwhile, SiO_2 formed in the HESAs after the introduction of Si. The stronger diffraction intensity of SiO_2 in the 2Si-HESA compared to the 1Si-HESA indicates that a higher concentration of SiO_2 was formed as the increasing Si content after long-term exposures.

3.4.2. Surface morphology

After being oxidized at 700 °C up to 480 h, two distinctly different types of oxides in terms of morphology and elemental composition formed through the entire surface of the 0Si-HESA, as shown in Fig. 7(a). The surface region with an area fraction of more than 96% was covered by Co-rich oxide humps in the 0Si-HESA, and the rest area was dominated by Cr- and Ti-rich planar oxides. These Co-rich oxides were determined to be Co_3O_4 [21], which is consistent with the XRD results in the current study. After adding 1 at% Si, despite that the aforementioned two types of oxides can still be observed, the area fraction of the Co-rich oxide humps was significantly reduced to ~37% (Fig. 7(b)). This is also in line with the current XRD results wherein the diffraction intensity of Co_3O_4 decreases with the increased Si content. Meanwhile, peaks of Si-containing oxides appear in the regions of planar oxides. As the Si content increases to 2 at%, the formation of Co-rich oxide humps was completely suppressed during the long-term exposure in the Ti-bearing HESAs. As can be seen in Fig. 7(c), nearly even oxidation occurs, and the constituent elements of oxides distribute almost uniformly through the whole surface of the oxidized 2Si-HESA.

3.4.3. Cross-sectional STEM-EDS analysis

To better understand the Si effect on the oxidation behavior, the cross-section of the oxide scales of the three HESAs after long-term exposure at 700 °C was further analyzed by STEM-EDS. The microstructure, elemental distribution, and phase analysis by SADP of the oxide layers after the long-term exposure at 700 °C for 480 h are shown in Figs. 8–10. The EDS maps reveal the distribution of all the elemental constituents in the oxide scale and the beneath alloy substrate. The formation and growth of the oxide scale consumed a certain amount of $L1_2$-forming elements of the neighboring alloy substrate, leading to the formation of an $L1_2$-depletion zone beneath the scale of all the HESAs. For the 0Si-HESA, the cross-sectional examination was conducted on the Co-rich oxide regions considering their frequent distribution on the oxide scale. The results in Fig. 8 show that the 0Si-HESA has multiple sublayers in the oxide scale with a total thickness of about 5.3 μm. At the gas/oxide interface, a Co-rich oxide layer is formed. Some regions of the Co-rich oxide layer are embedded with the Fe-rich oxide phase, which shows similar compositions with the oxides beneath the Co-rich oxide layer. Those Co-rich and Fe-rich oxides were determined to be spinel-structured Co_3O_4 and $Fe_2(Ni, Co)O_4$ oxide phases by SADP (Fig. 8(b)), which were also identified by XRD (Fig. 6). Meanwhile, Ni-rich (Ni, Co)O oxides were observed to intermittently distribute above or embed in the $Fe_2(Ni, Co)O_4$ oxide layer. Several pores formed within the above oxides, which can serve as short-circuit paths for oxygen diffusion. Below the $Fe_2(Ni, Co)O_4$ oxide layer, a Cr_2O_3 oxide layer with a thickness of up to 2.1 μm can be observed. As a solid-solute component, Ti and Al elements were observed to frequently mix in the Cr_2O_3 layer, which is similar to previous studies [21,22]. Some erose TiO_2 and Al_2O_3 oxides are irregularly distributed within the Cr_2O_3 layer, as evidenced by the EDS maps and SADPs. Meanwhile, discrete Al_2O_3 internal oxides were found to form below the Cr_2O_3 scale. The discontinuous Al_2O_3 cannot effectively hinder the inward diffusion of oxygen anions and the outward diffusion of metal cations.

Fig. 9(a) displays the typical STEM image and the corresponding EDS maps of the oxide scale with a total thickness of ~1 μm at the planar oxide region of the 1Si-HESA. The oxide constitution of the scale was identified by SADP, as shown in Fig. 9(b). In this case, the $Fe_2(Ni, Co)O_4$ spinel oxide is covered with a layer of TiO_2 at the outermost of the scale, and Cr_2O_3 and Al_2O_3 formed in the inner layer. Notably, discrete SiO_2 oxides were found to distribute above the Al_2O_3 layer, as shown in Fig. 9(c). Similar to that in the 0Si-HESA, irregular distribution of granular TiO_2 oxides was also observed in the Cr_2O_3 and Al_2O_3 layers. As the Si content further increases to 2 at%, the scale constitution of the alloy oxidized for 480 h remains unchanged compared to planar oxides of the 1Si-HESA, while the thickness decreases to ~650 nm, as shown in Fig. 10(a, b). Unlike the 0Si-HESA and 1Si-HESA, a continuous and compact Al_2O_3 layer with good adherence to the alloy substrate is revealed in the 2Si-HESA. The growth of the $Fe_2(Ni, Co)O_4$ spinel layer is significantly suppressed in the 2Si-HESA compared

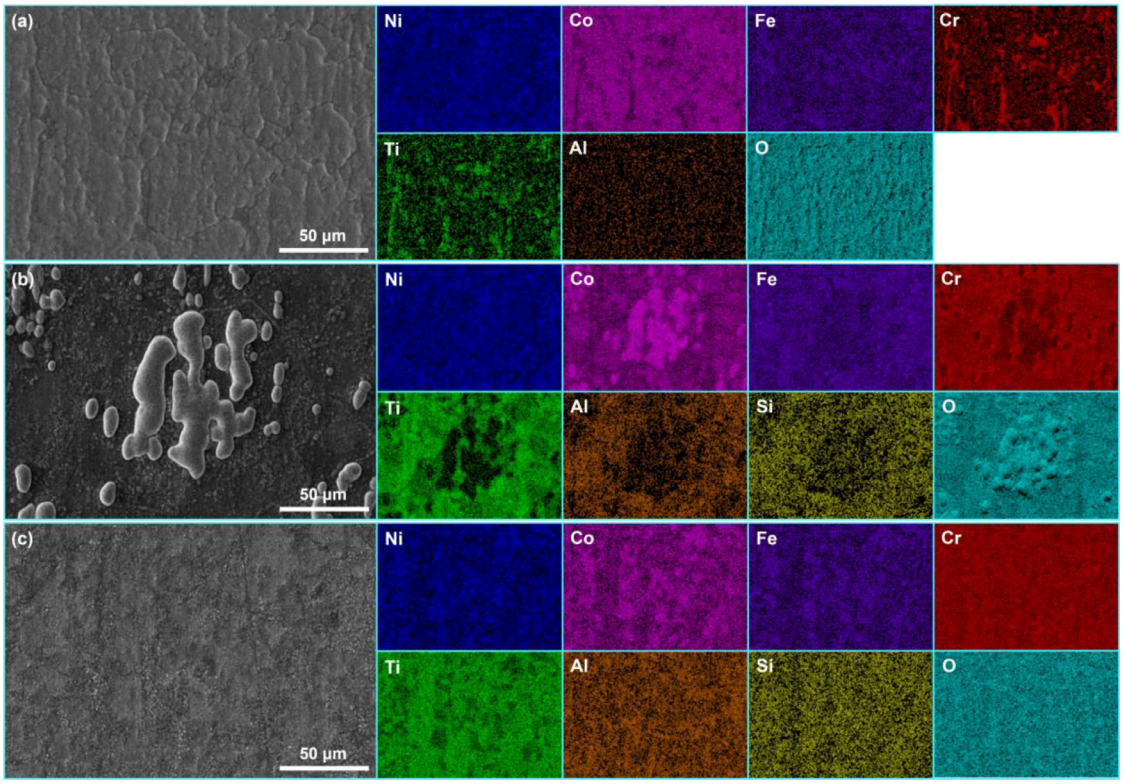

Fig. 7. Surface morphologies and corresponding elemental distributions of the (a) 0Si-HESA, (b) 1Si-HESA, and (c) 2Si-HESA after the oxidation at 700 °C for 480 h.

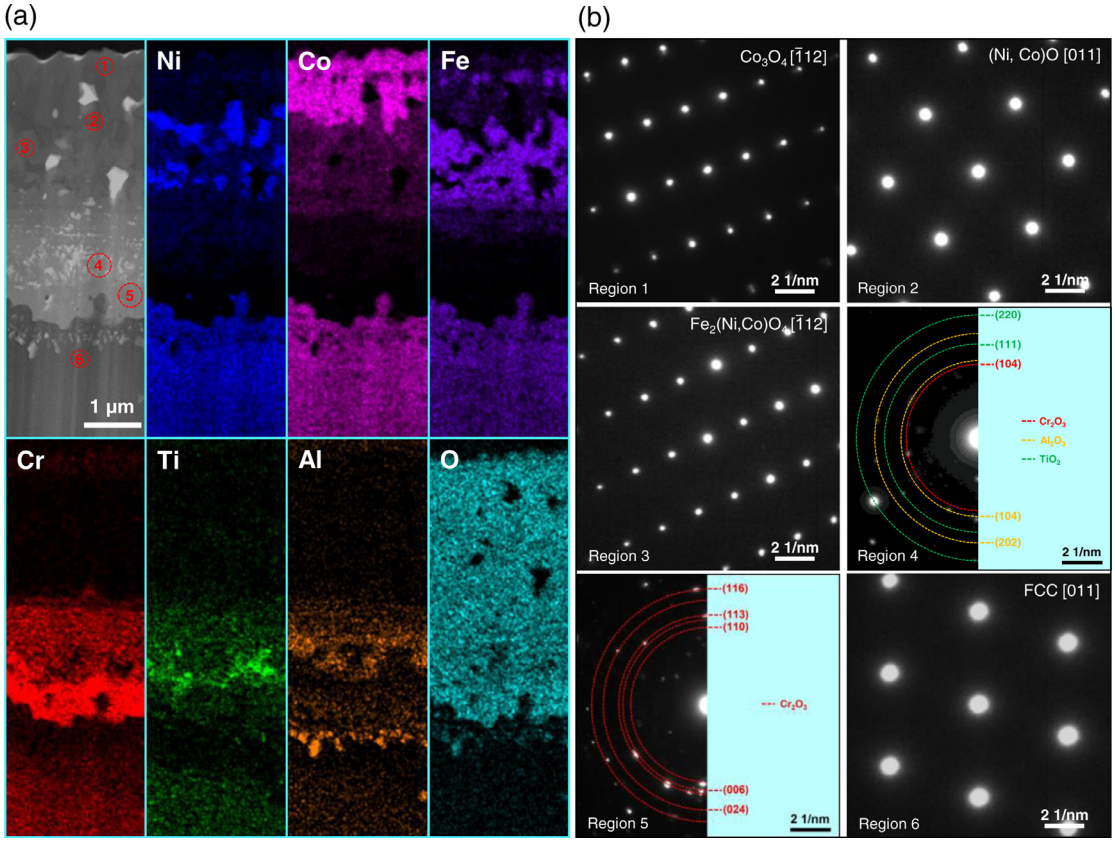

Fig. 8. (a) STEM image and corresponding elemental maps of the oxide layers of the 0Si-HESA after the oxidation at 700 °C for 480 h. (b) SADPs of the marked regions in (a).

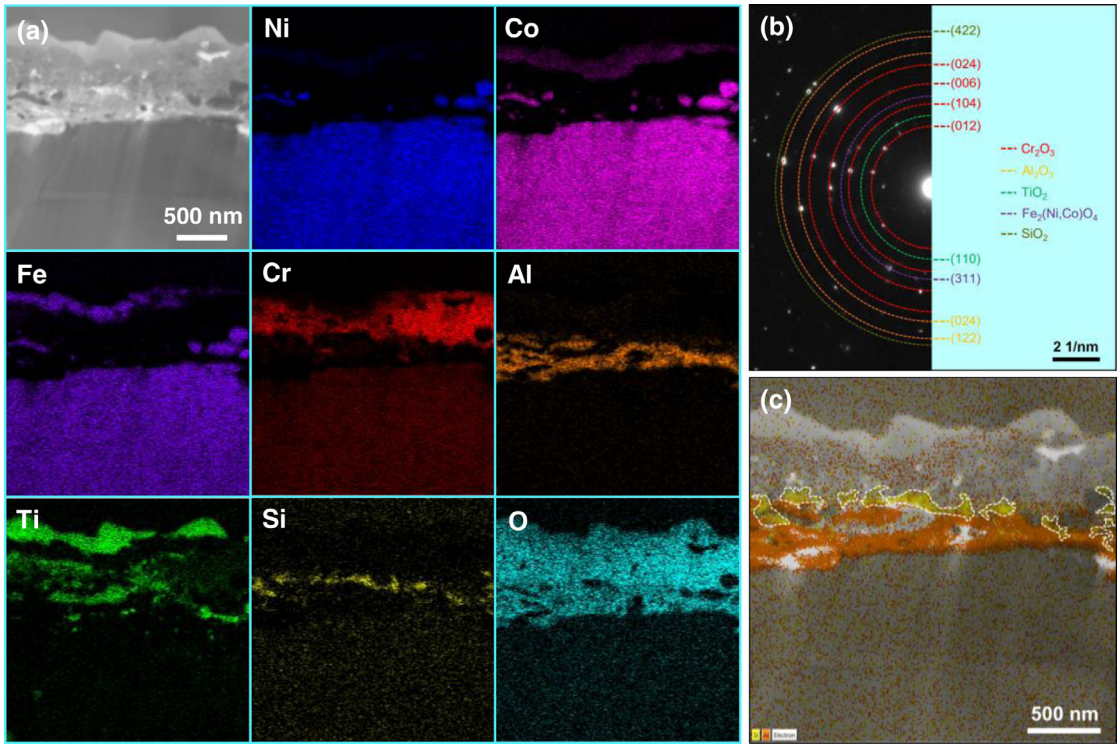

Fig. 9. (a) STEM image and corresponding elemental maps of the oxide layers of the 1Si-HESA after the oxidation at 700 °C for 480 h. (b) SADP of the oxide scale in (a). (c) STEM image revealing the distribution of Al and Si elements in the oxide scale, with the Si-rich oxides marked by white dotted lines.

to the other two HESAs, evidenced by its distinctly reduced thickness. Meanwhile, Si is also rich in the inner layer with a more amount than that in the 1Si-HESA. Unlike the 1Si-HESA, the SiO_2 oxides in the 2Si-HESA are observed to mix with the Al_2O_3 layer (Fig. 10(c)). It is worth noting that metal (Ni, Co, Fe) particles were observed between the Cr_2O_3 and Al_2O_3 layers in the 0Si-HESA and 1Si-HESA, but not in the 2Si-HESA. The presence of these metal particles can be attributed to the outward diffusion of Ni, Co, and Fe ions from the matrix through the Al_2O_3 layer, resulting from the large compressive stresses generated by the volume increase related to the discontinuous Al_2O_3 [39]. This phenomenon further demonstrates the effective protectiveness against the outward diffusion of cations of the SiO_2 and Al_2O_3 layers in the 2Si-HESA. It is plausible that the thickness reduction of the oxide scale with the increasing Si content in the HESAs was attributed to the formation of SiO_2 and continuous Al_2O_3 layers, which effectively retards the outward diffusion of metal cations and inward diffusion of oxygen anions.

4. Discussion

In the present study, we systematically investigated the oxidation behavior and mechanical properties of Si-doped Ti-bearing HESAs. The results demonstrate that Si is an ideal alloying element for improving both tensile ductility and oxidation resistance at 700 °C. As a result, rationalization of the above findings is necessarily required to uncover the underlying mechanisms.

4.1. On the intermediate-temperature ductility

The severe embrittlement of alloys at intermediate temperatures can generally be attributed to the environmental oxygen attack [20,40,41]. At elevated temperatures in the air, high-energy GBs usually act as preferential diffusion paths for oxygen penetration [41–43]. The segregation of the embrittling oxygen atoms would lead to the decohesion of metallic bonds, giving rise to the premature onset of intergranular cracking at local GBs during tensile deformation [44,45]. Such a phenomenon has also been widely observed in conventional pure Ni, superalloys, and intermetallic alloys [41,46,47]. For example, compared with the commercially pure Ni270 after being exposed to air at elevated temperatures, the same material treated with similar conditions but exposed to vacuum displayed much higher tensile ductility at temperatures from 25 to 1000 °C, with the ductility minimum occurring around 700 °C for both materials [46]. Further investigations indicated that the formation of external oxide along GBs can be the main reason for this embrittlement. Meanwhile, previous studies revealed that compared to superalloys deformed in the air at intermediate temperatures, substantial ductility recovery can be achieved when the materials were deformed in an inert argon atmosphere [40]. The elimination of external oxidation damages would restrain the dynamic intergranular embrittlement, thus remarkably reducing the stress concentration along GBs upon tensile loading.

Based on the above analyses, we investigated the elemental distribution near the GBs of the 1Si-HESA and 2Si-HESA after 10 min of exposure in the air at 700 °C, as shown in Figs. 11 and 12, respectively. For the 1Si-HESA, a two-layer oxide scale with an average thickness of ~80 nm, consisting of the outer $Fe_2(Ni, Co)O_4$ layer and the inner Cr_2O_3 layer, was formed on the surface of the grain bulk. Notably, an oxide protrusion can be observed to extend inward to a depth of ~110 nm near the GB. On the front of the oxide protrusion, oxygen continues to penetrate inwards along the GB to as far as ~623 nm apart from the oxide-metal interface. As the Si content increases to 2 at%, the initial scale constitution on the surface of the grain bulk is the same as that of the 1Si-HESA, but with a slightly reduced thickness of ~65 nm. A Ti-rich oxide island was formed on the top of the intergranular G phase, attributed to the high Ti concentration in the G phase (Fig. 2) and the low Gibbs formation energies of TiO_2 (i.e., –767.6 kJ mol^{-1}, O_2 at 700 °C [48]). In strong contrast with the 1Si-HESA, no internal extended oxide

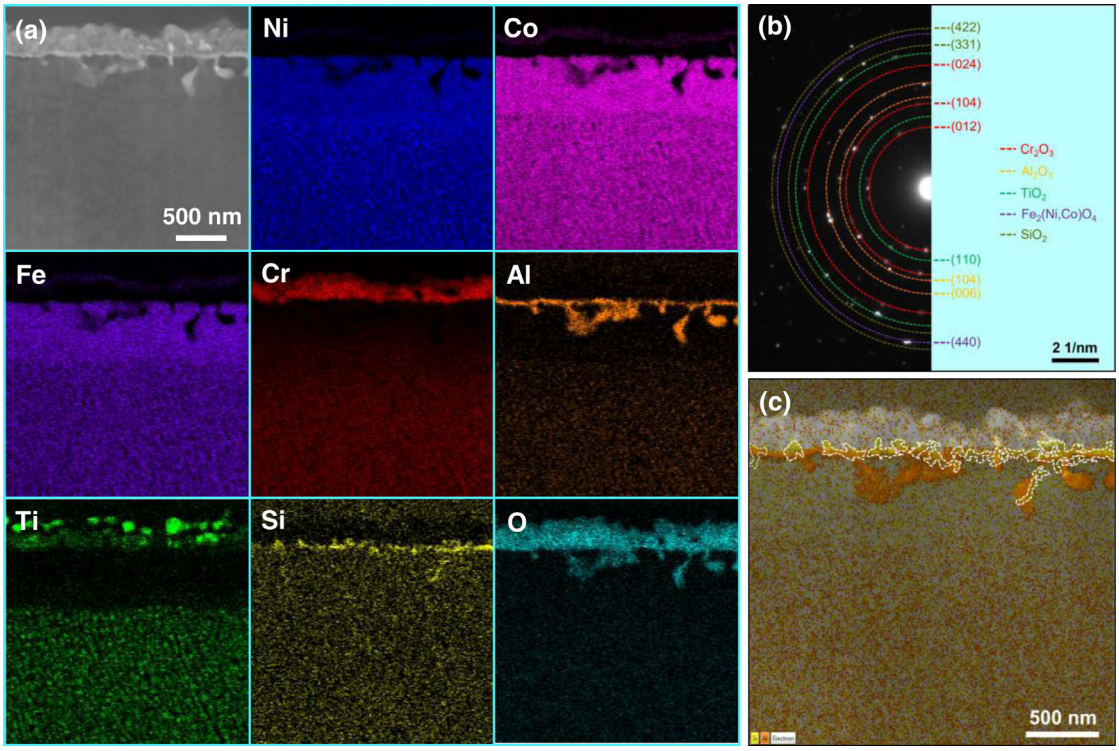

Fig. 10. (a) STEM image and corresponding elemental maps of the oxide layers of the 2Si-HESA after the oxidation at 700 °C for 480 h. (b) SADP of the oxide scale in (a). (c) STEM image revealing the distribution of Al and Si elements in the oxide scale, with the Si-rich oxides marked by white dotted lines.

protrusion can be clearly observed in the 2Si-HESA. Oxygen only diffuses inward to a total distance of ~204 nm along the GB of the 2Si-HESA, by forming Ti-rich oxide (presumably TiO_2) on the side of the G phase. It has been reported that the continuous TiO_2 oxides formed alongside the crack tip can act as a protective layer to hinder further oxygen penetration [41]. Apparently, the G phase in the 2Si-HESA can serve as an effective barrier for the inward diffusion of oxygen along GBs. During deformation, tensile stress-assisted oxygen diffusion tends to be facilitated along GBs ahead of the crack tip [44,49]. The dynamic embrittlement of GBs resulting from such a stress-controlled oxygen penetration will lead to fast brittle intercrystalline crack propagation. It is suggested that compared with the other two HESAs, the oxygen-induced dynamic embrittlement behavior in the 2Si-HESA tends to be alleviated due to the existence of the intergranular G phase. Therefore, the intergranular crack initiation and propagation can be suppressed to some extent, resulting in improved strength-ductility synergy in the 2Si-HESA at intermediate temperatures.

4.2. On the long-term oxidation mechanism

Based on the aforementioned results, the scale constitution formed on the Ti-bearing HESAs was optimized by Si additions. The STEM-EDS results revealed that a transition from complex oxide compositions dominated by both spinel-type (Co_3O_4 and $Fe_2(Ni, Co)O_4$) and corundum-type (Cr_2O_3 and Al_2O_3) oxides toward simpler ones dominated by corundum-type (Cr_2O_3 and Al_2O_3) oxides was affected by the presence of Si. Meanwhile, the introduction of Si in the HESAs facilitates the formation of SiO_2 below the Cr_2O_3 layers, which promotes a compact oxide scale and is advantageous to the improvement of oxidation resistance [50–52].

Thermodynamically, the standard Gibbs formation energies (ΔG_f^o) of the relevant oxides at 700 °C were reported to be in the following sequence: Al_2O_3 (–913.4 kJ/mol, O_2) < TiO_2 (–767.6 kJ/mol, O_2) < SiO_2 (–735.8 kJ/mol, O_2) < Cr_2O_3 (–588.7 kJ/mol, O_2) < Fe_2O_3 (–378.8 kJ/mol, O_2) < CoO (–331.2 kJ/mol, O_2) < NiO (–303.7 kJ/mol, O_2) < Co_3O_4 (–268.2 kJ/mol, O_2) [48]. Theoretically, the formation of Al_2O_3 and SiO_2 is relatively easy due to the strong oxygen affinity of Al and Si. However, the related oxides did not form at the preliminary oxidation process stage, which can be attributed to the low concentration of Al and Si elements in the HESAs. Due to the kinetics reasons, oxygen atoms chemically absorb on the surface of materials and react with principal element cations to form the Cr_2O_3 and $Fe_2(Ni, Co)O_4$ oxide scale initially (Figs. 11 and 12). During the inward migration of oxygen, the oxide scale consumes the penetrative oxygen gradually, generating an oxygen potential gradient along the penetration depth. With prolonged exposure, the outermost oxide scale grows continuously and oxygen transportation through the scale becomes considerably difficult, leading to a decreased oxygen pressure at the oxide-to-metal interface. Subsequently, the diffusion-controlled internal oxidation of SiO_2 and Al_2O_3 occurs at a low oxygen partial pressure.

The advantageous role of Si addition on the oxidation resistance of the studied HESAs can be attributed to several factors. The rapid growth of unprotective Fe-rich oxides has been widely revealed to be one critical factor for the inferior oxidation resistance of many HEA systems [22,53,54]. Huang et al. [53] reported that the formation of Fe-rich oxides at the outmost oxide layer of an $Al_{0.3}CuCrFeNi_2$ HEA at 600 °C can be attributed to the fast diffusion coefficient of Fe cations through the Cr_2O_3 layer. In the current study, both the existence of SiO_2 and Si-rich intergranular precipitates can suppress the outward diffusion of Fe cations during oxidation. The diffusion coefficient of Fe in SiO_2 and Cr_2O_3 can be given as the following equations [55,56]:

$$D_{SiO2}^{Fe} = 6 \times 10^{-3} \exp\left(\frac{-288960}{RT}\right) \quad (2)$$

$$D_{Cr2O3}^{Fe} = 7 \times 10^{-4} \exp\left(\frac{-245000}{RT}\right) \quad (3)$$

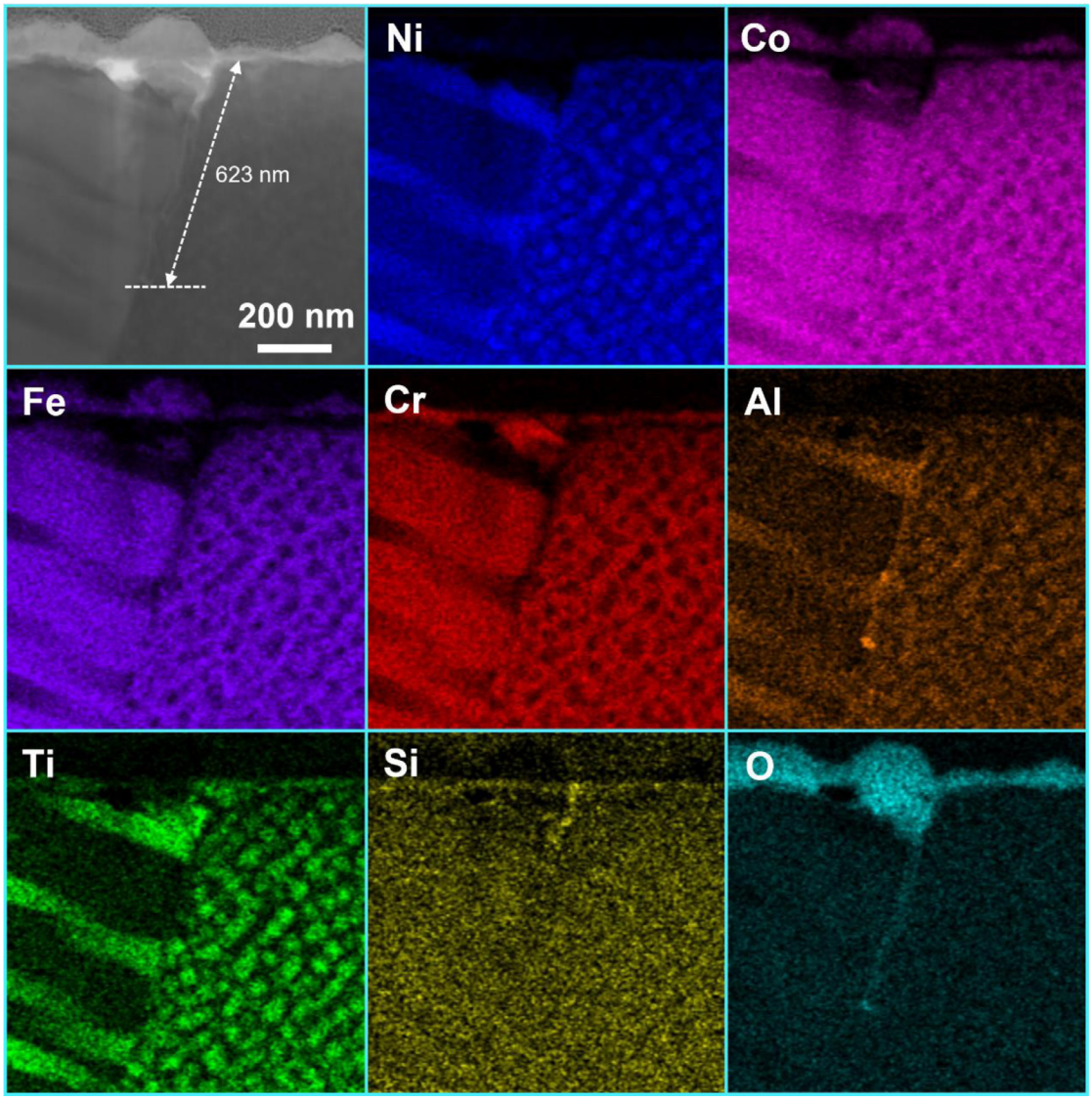

Fig. 11. STEM image and corresponding elemental maps near the GB of the 1Si-HESA after the oxidation at 700 °C for 10 min.

where R is the molar gas constant, and T is the temperature. At the current studied temperature of 700 °C (973 K), D^{Fe}_{SiO2} is 1.845×10^{-18} cm^2 s^{-1} and D^{Fe}_{Cr2O3} is 4.930×10^{-17} cm^2 s^{-1}. Apparently, SiO_2 displays a more significant blocking effect than Cr_2O_3 towards the outward diffusion of Fe. Meanwhile, the intergranular G phase can act strong diffusion barrier of Cr and Fe cations because of the extremely low solubility of Cr and Fe in the G phase (Fig. 2(e, f)), thus their outward diffusion via GBs is significantly suppressed in the 2Si-HESA. At the current studied temperature, i.e., 700 °C, GBs are regarded as the primary channels for the outward transportation of metal cations [57,58]. Hence, the growth of Cr_2O_3 and $Fe_2(Ni, Co)O_4$ tends to be remarkably restrained during long-term exposure.

In addition to the formation of SiO_2 and intergranular Si-rich G phases, the introduction of Si promotes the continuity of Al_2O_3. Generally, fast internal oxidation progress of Al_2O_3 would occur at the oxide-metal interface in alloys with a low Al concentration when the oxygen activity is relatively high, leading to the formation of discontinuous Al_2O_3 [22,59]. In the current study, the formation of SiO_2 below the Cr_2O_3 can significantly reduce the oxygen partial pressure due to the high affinity between Si and O, resulting in low partial oxygen pressure across the oxide film and matrix interfaces. Meanwhile, sufficient SiO_2 particles formed at the early oxidation stage can serve as nucleation sites for the formation of Al_2O_3, as evidenced by Fig. 10(c). That is, adequate Si addition can increase the selective oxidation of Al, reducing the critical concentration of Al and enhancing the formation of continuous Al_2O_3. The outward diffused cations tend to be suppressed dramatically due to the formation of a continuous mixture of SiO_2 and Al_2O_3 in the 2Si-HESA. The suppressed outward diffusion of cations, especially Ti and Fe cations (Fig. 10), would reduce the diffusion channels by decreasing the number of vacancies left by cations, subsequently restraining the inward diffusion of oxygen and thus improving the oxidation resistance. It is reasonable that the oxidation resistance of the low Si-containing HESA, i.e., the 1Si-HESA, cannot be significantly improved due to the inadequate amount of SiO_2, which cannot effectively restrain the diffusion of both metal cations and oxygen anions, and also provide insufficient nucleation sites for the formation of continuous Al_2O_3. Even if not very continuous, the SiO_2 particles formed in the 1Si-HESA still reduced the oxidation rate when compared to the 0Si-HESA. Meanwhile, the addition of Si was also reported to be beneficial for the formation of a more homogeneous and compact Cr_2O_3 film [60]. This is consistent with the current results that the Cr_2O_3 layer ex-

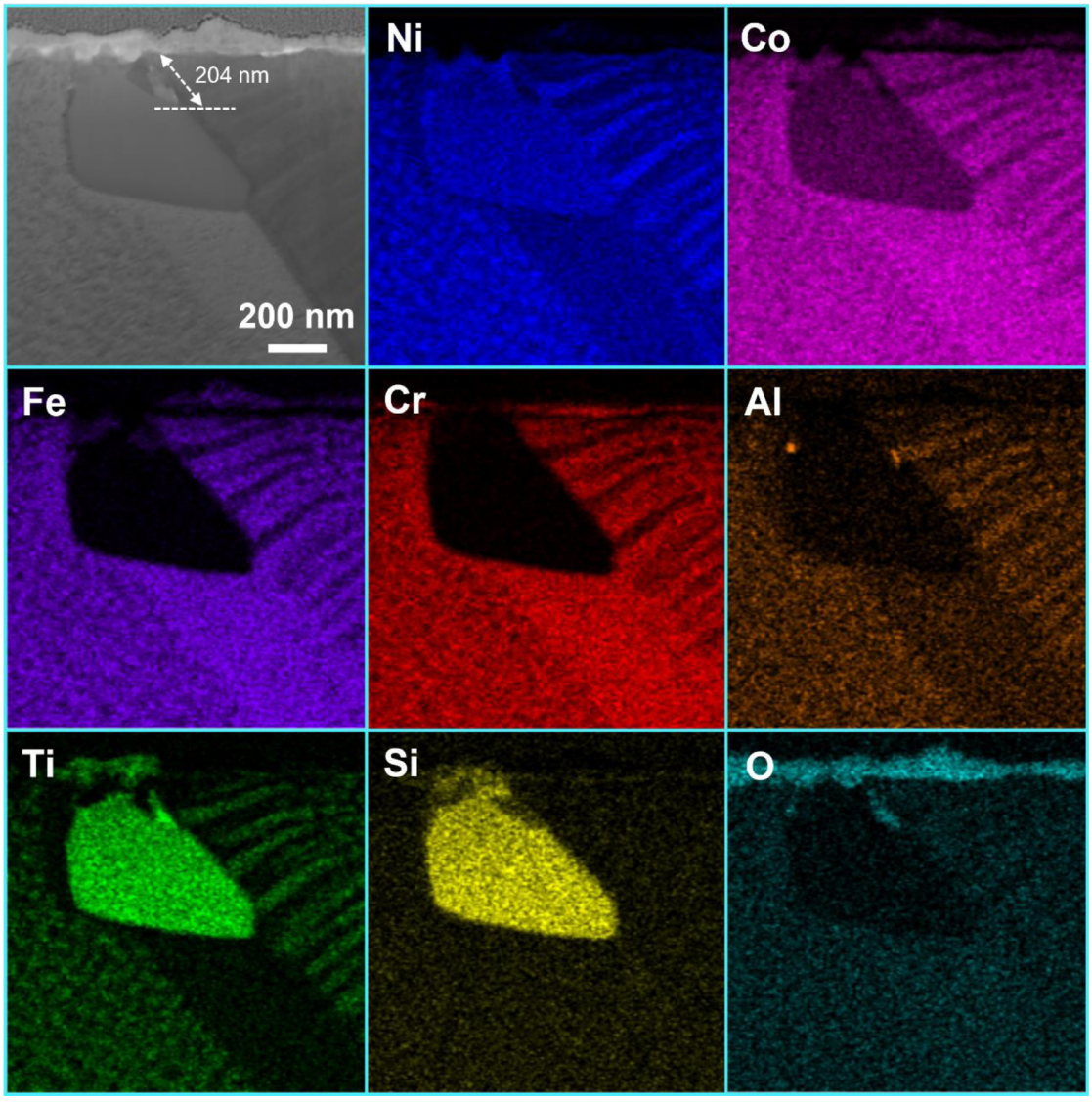

Fig. 12. STEM image and corresponding elemental maps near the GB of the 2Si-HESA after the oxidation at 700 °C for 10 min.

hibits fewer gaps in the HESAs with higher Si contents, which suppresses the cation diffusion from the matrix to the oxide, and also the inward diffusion of oxygen anions through the gaps.

Based on the above discussion, the existence of Si in the matrix and the formation of Si-rich intergranular precipitates in the Ti-bearing HESAs can both effectively hinder the outward diffusion of metal cations. This can offset the degradation effect of Ti, thus improving the overall oxidation resistance of the HESAs. The findings in the current study are suggested to be supportive of the future engineering design of high-performance HESAs for elevated temperature applications through elaborate alloying design.

5. Conclusion

In this study, the effect of minor additions of Si on the mechanical properties and oxidation behavior of $(Ni_2Co_2FeCr)_{92-x}Ti_4Al_4Si_x$ (x = 0, 1, and 2 at%) HESAs at 700 °C were systematically investigated. Microstructures of the studied HESAs were carefully characterized by combining SEM, APT, and TEM. The results demonstrate that Si addition is an effective alloying scheme to simultaneously improve the tensile ductility and oxidation resistance of Ti-bearing HESAs at intermediate temperatures. Based on our observations, the conclusion can be reached as follows:

(1) The microstructure analyses reveal that a typical "FCC + $L1_2$" dual-phase structure can be obtained in the current $(Ni_2Co_2FeCr)_{92}Ti_4Al_4$ and $(Ni_2Co_2FeCr)_{91}Ti_4Al_4Si_1$ HESAs. As the Si content increases to 2 at%, (Ni, Ti, Si)-rich G phase precipitates on the GBs.

(2) The intergranular G phase in the $(Ni_2Co_2FeCr)_{90}Ti_4Al_4Si_2$ HESA can effectively suppress the long-distance inward diffusion of oxygen along GBs, thus improving the intermediate-temperature embrittlement to some extent. Compared with $(Ni_2Co_2FeCr)_{92}Ti_4Al_4$ HESA, the ultimate tensile strength of the $(Ni_2Co_2FeCr)_{90}Ti_4Al_4Si_2$ HESA increased from 808 to 870 MPa, and the ductility increased from ~8.3% to ~ 13.4%.

(3) The formation of SiO_2 during long-term oxidation and the intergranular G phase in $(Ni_2Co_2FeCr)_{90}Ti_4Al_4Si_2$ HESA can effectively suppress the outward diffusion of cations, thus significantly improving the oxidation resistance by suppressing the growth of spinel-type oxides and chromium oxides. Compared to the $(Ni_2Co_2FeCr)_{92}Ti_4Al_4$ HESA, the parabolic-rate constant of the $(Ni_2Co_2FeCr)_{90}Ti_4Al_4Si_2$ HESA decreases from 1.02×10^{-3} to 2.54×10^{-4} $mg^2\ cm^{-4}\ h^{-1}$.

Acknowledgements

The authors from the City University of Hong Kong are grateful for the financial support from Hong Kong Research Grant Council (RGC) (Grant Nos. CityU 11214820, CityU 11209021, CityU 21205621, CityU 9360161 and C1017-21G), the National Natural Science Foundation of China (Grant Nos. 52101151 and 52101162), and the Shenzhen Science and Technology Program (Grant No. SGDX20210823104002016). Zengbao Jiao from the Hong Kong Polytechnic University thanks the financial support from Hong Kong RGC (Grant Nos. 25202719 and 15227121). Yilu Zhao from the Harbin Institute of Technology (Shenzhen) acknowledges the financial support from National Natural Science Foundation of China (Grant No. 52101135) and the Shenzhen Science and Technology Program (Grant No. RCBS20210609103202012).

Supplementary materials

Supplementary material associated with this article can be found, in the online version, at doi:10.1016/j.jmst.2023.01.044.

References

[1] E.P. George, D. Raabe, R.O. Ritchie, Nat. Rev. Mater. 4 (2019) 515–534.
[2] B. Gludovatz, A. Hohenwarter, D. Catoor, E.H. Chang, E.P. George, R.O. Ritchie, Science 345 (2014) 1153–1158.
[3] Z.F. Lei, X.J. Liu, Y. Wu, H. Wang, S.H. Jiang, S.D. Wang, X.D. Hui, Y.D. Wu, B. Gault, P. Kontis, D. Raabe, L. Gu, Q. Zhang, H. Chen, H. Wang, J. Liu, K. An, Q. Zeng, T.G. Nieh, Z. Lu, Nature 563 (2018) 546–550.
[4] Z.Z. Li, S.T. Zhao, R.O. Ritchie, M.A. Meyers, Prog. Mater. Sci. 102 (2019) 296–345.
[5] Y. Zhang, T.T. Zuo, Z. Tang, M.C. Gao, K.A. Dahmen, P.K. Liaw, Z.P. Lu, Prog. Mater. Sci. 61 (2014) 1–93.
[6] B.X. Cao, H.J. Kong, Z.Y. Ding, S.W. Wu, J.H. Luan, Z.B. Jiao, J. Lu, C.T. Liu, T. Yang, Scr. Mater. 199 (2021) 113826.
[7] J. Chen, X.Y. Zhou, W.L. Wang, B. Liu, Y.K. Lv, W. Yang, D.P. Xu, Y. Liu, J. Alloy. Compd. 760 (2018) 15–30.
[8] J.Y. He, N. Li, S.K. Makineni, Y.S. Zhao, W.H. Liu, L. Wang, Z.W. Wang, M. Song, Mater. Sci. Eng. A 851 (2022) 143610.
[9] Y.L. Zhao, T. Yang, Y.R. Li, L. Fan, B. Han, Z.B. Jiao, D. Chen, C.T. Liu, J.J. Kai, Acta Mater. 188 (2020) 517–527.
[10] B.X. Cao, W.W. Xu, C.Y. Yu, S.W. Wu, H.J. Kong, Z.Y. Ding, T.L. Zhang, J.H. Luan, B. Xiao, Z.B. Jiao, Y. Liu, T. Yang, C.T. Liu, Acta Mater. 229 (2022) 117763.
[11] T. Yang, Y.L. Zhao, Y. Tong, Z.B. Jiao, J. Wei, J.X. Cai, X.D. Han, D. Chen, A. Hu, J.J. Kai, K. Lu, Y. Liu, C.T. Liu, Science 362 (2018) 933–937.
[12] Y. Tong, D. Chen, B. Han, J. Wang, R. Feng, T. Yang, C. Zhao, Y.L. Zhao, W. Guo, Y. Shimizu, C.T. Liu, P.K. Liaw, K. Inoue, Y. Nagai, A. Hu, J.J. Kai, Acta Mater. 165 (2019) 228–240.
[13] T. Yang, Y.L. Zhao, L. Fan, J. Wei, J.H. Luan, W.H. Liu, C. Wang, Z.B. Jiao, J.J. Kai, C.T. Liu, Acta Mater. 189 (2020) 47–59.
[14] B. Xiao, J. Luan, S. Zhao, L. Zhang, S. Chen, Y. Zhao, L. Xu, C.T. Liu, J.J. Kai, T. Yang, Nat. Commun. 13 (2022) 4870.
[15] Y.Y. Zhao, H.W. Chen, Z.P. Lu, T.G. Nieh, Acta Mater. 147 (2018) 184–194.
[16] J.Y. He, H. Wang, H.L. Huang, X.D. Xu, M.W. Chen, Y. Wu, X.J. Liu, T.G. Nieh, K. An, Z.P. Lu, Acta Mater. 102 (2016) 187–196.
[17] M.R. Barnett, M. Senadeera, D. Fabijanic, K.F. Shamlaye, J. Joseph, S.R. Kada, S. Rana, S. Gupta, S. Venkatesh, Acta Mater. 200 (2020) 735–744.
[18] J. Joseph, M. Annasamy, S.R. Kada, P.D. Hodgson, M.R. Barnett, D.M. Fabijanic, Mater. Sci. Eng. A 835 (2022) 142620.
[19] S.W. Wu, T. Yang, B.X. Cao, J.H. Luan, Y.F. Jia, L. Xu, Y.K. Mu, T.L. Zhang, H.J. Kong, X. Tong, J.C. Peng, G. Wang, Q.J. Zhai, J. Lu, C.T. Liu, Scr. Mater. 204 (2021) 114066.
[20] J.X. Hou, S.F. Liu, B.X. Cao, J.H. Luan, Y.L. Zhao, Z. Chen, Q. Zhang, X.J. Liu, C.T. Liu, J.J. Kai, T. Yang, Acta Mater. 238 (2022) 118216.
[21] S.F. Liu, W. Kai, J.X. Hou, Y.L. Zhao, Q. Li, C.H. Yang, T. Yang, J.J. Kai, Corros. Sci. 206 (2022) 110499.
[22] Z.Y. Ding, B.X. Cao, J.H. Luan, Z.B. Jiao, Corros. Sci. 184 (2021) 109365.
[23] M. Bensch, J. Preußner, R. Hüttner, G. Obigodi, S. Virtanen, J. Gabel, U. Glatzel, Acta Mater. 58 (2010) 1607–1617.
[24] H.Q. Pei, Z.X. Wen, Y.M. Zhang, Z.F. Yue, Appl. Surf. Sci. 411 (2017) 124–135.
[25] G.L. Wang, Y. Sun, X.G. Wang, J.D. Liu, J.L. Liu, J.G. Li, J.J. Yu, Y.Z. Zhou, T. Jin, X. Sun, X.D. Sun, J. Mater. Sci. Technol. 33 (2017) 1219–1226.
[26] T.K. Tsao, A.C. Yeh, C.M. Kuo, H. Murakami, Entropy 18 (2016) 62.
[27] J.Y. Zhang, B. Xiao, Q. Li, B.X. Cao, J.X. Hou, S.F. Liu, J.X. Zhang, W.C. Xiao, J.H. Luan, Y.L. Zhao, C.T. Liu, T. Yang, J. Alloy. Compd. 918 (2022) 165597.
[28] D.X. Wei, L.Q. Wang, Y.J. Zhang, W. Gong, T. Tsuru, I. Lobzenko, J. Jiang, S. Harjo, T. Kawasaki, J.W. Bae, W. Lu, Z. Lu, Y. Hayasaka, T. Kiguchi, N.L. Okamoto, T. Ichitsubo, H.S. Kim, T. Furuhara, E. Ma, H. Kato, Acta Mater. 225 (2022) 117571.
[29] S.F. Liu, W.T. Lin, Y.L. Zhao, D. Chen, G. Yeli, F. He, S.J. Zhao, J.J. Kai, J. Alloy. Compd. 844 (2020) 156162.
[30] W. Kai, F.P. Cheng, C.Y. Liao, C.C. Li, R.T. Huang, J.J. Kai, Mater. Chem. Phys. 210 (2018) 362–369.
[31] Z.Q. Xu, Z.L. Ma, Y. Tan, X.W. Cheng, Scr. Mater. 206 (2022) 114230.
[32] M.Y. Ma, A.H. Han, Z.J. Zhang, Y. Lian, C. Zhao, J. Zhang, Corros. Sci. 185 (2021) 109417.
[33] Y.L. Zhao, T. Yang, Y. Tong, J. Wang, J.H. Luan, Z.B. Jiao, D. Chen, Y. Yang, A. Hu, C.T. Liu, J.J. Kai, Acta Mater. 138 (2017) 72–82.
[34] J.Y. He, H. Wang, Y. Wu, X.J. Liu, H.H. Mao, T.G. Nieh, Z.P. Lu, Intermetallics 79 (2016) 41–52.
[35] C. Kienl, F.D. León-Cázares, C.M.F. Rae, Acta Mater. 225 (2022) 115743.
[36] B.G. Mendis, I.P. Jones, R.E. Smallman, J. Electron. Microsc. 53 (2004) 311–323.
[37] C. Wagner, J. Electrochem. Soc. 99 (1952) 369.
[38] G.A. El-Awadi, S. Abdel-Samad, E.S. Elshazly, Appl. Surf. Sci. 378 (2016) 224–230.
[39] G.D. Jia, W.J. Xu, M.H. Ouyang, H.C. Wang, L.B. Wang, X.S. Xiao, Corros. Sci. 187 (2021) 109475.
[40] B.X. Cao, D.X. Wei, X.F. Zhang, H.J. Kong, Y.L. Zhao, J.X. Hou, J.H. Luan, Z.B. Jiao, Y. Liu, T. Yang, C.T. Liu, Mater. Today Phys. 24 (2022) 100653.
[41] A.A.N. Németh, D.J. Crudden, D.E.J. Armstrong, D.M. Collins, K. Li, A.J. Wilkinson, C.R.M. Grovenor, R.C. Reed, Acta Mater. 126 (2017) 361–371.
[42] J. Ju, Z. Shen, M.D. Kang, J.Q. Zhang, J. Wang, Corros. Sci. 199 (2022) 110203.
[43] H.S. Kitaguchi, H.Y. Li, H.E. Evans, R.G. Ding, I.P. Jones, G. Baxter, P. Bowen, Acta Mater. 61 (2013) 1968–1981.
[44] J.A. Pfaendtner, C.J. McMahon Jr, Acta Mater. 49 (2001) 3369–3377.
[45] H.J. Christ, K. Wackermann, U. Krupp, Mater. High Temp. 33 (2016) 528–535.
[46] R.H. Bricknell, D.A. Woodford, Metall. Trans. A 12 (1981) 425–433.
[47] C.T. Liu, C.L. White, Acta Metall. 35 (1987) 643–649.
[48] I. Barin, G. Platzki, Thermochemical Data of Pure Substances, VCh, Weinheim, 1989.
[49] L. Viskari, M. Hörnqvist, K.L. Moore, Y. Cao, K. Stiller, Acta Mater. 61 (2013) 3630–3639.
[50] J. Jing, J. He, H.B. Guo, J. Mater. Sci. Technol. 35 (2019) 2038–2047.
[51] A. Sato, Y.L. Chiu, R.C. Reed, Acta Mater. 59 (2011) 225–240.
[52] P. Tunthawiroon, M. Kitiwan, K. Srirussamee, Y. Li, K. Yamanaka, A. Chiba, Corros. Sci. 191 (2021) 109753.
[53] G.Q. Huang, J. Wu, R. Yuan, Y.X. Li, F.Q. Meng, P.H. Lei, C.Y. Lu, F.J. Cao, Y.F. Shen, Corros. Sci. 195 (2022) 109984.
[54] Y. Yin, Q.Y. Tan, Y.T. Zhao, Q. Sun, Z.M. Shi, M. Bermingham, W. Zhuang, H. Huang, M.X. Zhang, Corros. Sci. 180 (2021) 109190.
[55] A. Atkinson, J.W. Gardner, Corros. Sci. 21 (1981) 49–58.
[56] A.C.S. Sabioni, A.M. Huntz, F. Silva, F. Jomard, Mater. Sci. Eng. A 392 (2005) 254–261.
[57] P. Tunthawiroon, Y. Li, N. Tang, Y. Koizumi, A. Chiba, Corros. Sci. 95 (2015) 88–99.
[58] L. Klein, B. von Bartenwerffer, M.S. Killian, P. Schmuki, S. Virtanen, Corros. Sci. 79 (2014) 29–33.
[59] Y.Z. Li, F. Pyczak, J. Paul, Z.K. Yao, J. Mater. Sci. Technol. 34 (2018) 2212–2217.
[60] P. Tunthawiroon, Y. Li, A. Chiba, Corros. Sci. 100 (2015) 428–434.